Applied Catalysis B: Environmental 184 (2016) 20–27

Contents lists available at ScienceDirect

Applied Catalysis B: Environmental

journal homepage: www.elsevier.com/locate/apcatb

Efficient visible light photocatalytic heterostructure of nonstoichiometric bismuth oxyiodide and iodine intercalated $Bi_2O_2CO_3$

Mingce Long[a,*], Peidong Hu[a], Haodong Wu[b], Jun Cai[a], Beihui Tan[a], Baoxue Zhou[a]

[a] School of Environmental Science and Engineering, Shanghai Jiao Tong University, 800 Dong Chuan Road, Shanghai 200240, PR China
[b] Identity Environmental Technology (Shanghai) Co., Ltd., 555 Dong Chuan Road, Shanghai 200241, PR China

ARTICLE INFO

Article history:
Received 17 September 2015
Received in revised form 1 November 2015
Accepted 18 November 2015
Available online 28 November 2015

Keywords:
Photocatalysis
Bismuth oxyiodide
Visible light
Heterostructure
Intercalations

ABSTRACT

Bismuth oxide based (BOB) materials display strong potentials in visible light photocatalytic applications, but are greatly restricted by the poor stability for organic degradation in aqueous solutions. Herein, a unique heterostructural photocatalyst, nonstoichiometric bismuth oxyiodide $Bi_2O_{3-x}I_{2x}$($x = 0.243$) covered with iodine intercalated $Bi_2O_2CO_3$, were developed through a treatment of $Bi_7O_9I_3$ in urea solution and subsequent calcinations. The interesting formation chemistry of this heterostructure were revealed and their dramatically enhanced photoresponse properties were studied. The lower amount of iodine in $Bi_2O_{3-x}I_{2x}$ contributes a higher oxidation potential of photogenerated holes, while the presence of outlayer of iodine intercalated $Bi_2O_2CO_3$ retards the transformation of inner bismuth oxyiodide. We anticipate this strategy can be generalized to tune iodine contents and to fabricate delicate BOB photocatalytic heterostructures with desirable performance for environmental applications.

1. Introduction

Bismuth oxide based (BOB) materials are promising candidates for photocatalytic applications, because of the relative abundance of elementary bismuth and the possibility of visible light driven reactions. Among these materials, bismuth oxyiodide and bismuth oxide have attracted increasing attention. The former is a family of V–VI–VII ternary oxides, including BiOI and other oxygen rich compounds, such as $Bi_4O_5I_2$, $Bi_7O_9I_3$ and Bi_5O_7I [1–5]. The formula of these compounds can be generalized as $Bi_2O_{3-x}I_{2x}$ ($x = 1, 0.5, 0.428, 0.2$, etc.), in which iodine anions are regarded as the intercalators in the interweaved space of bismuth oxides. Meanwhile, most bismuth oxide polymorphs display visible light photocatalytic activity, including α, β, γ and δ-Bi_2O_3 [6–12]. However, these $Bi_2O_{3-x}I_{2x}$ or Bi_2O_3 compounds are greatly restricted by the poor stability during the photocatalytic degradation of organic pollutants. The frequent transformation product is bismuth oxide carbonates ($Bi_2O_2CO_3$), because of its relatively negative formation enthalpy and the available carbonates generated from dissolved CO_2 or the mineralization of organics in aqueous solution [13]. However, the appearance of the wide bandgap $Bi_2O_2CO_3$ ($E_g = 3.31$ eV) would significantly decrease the visible light photocatalytic activity. However, $Bi_2O_2CO_3$ is a more stable photocatalyst with a similar layered crystal structure as BiOI, in which carbonate anions intercalate in the interlayer of $[Bi_2O_2]^{2+}$ structure [14,15]. It can be expected that the intercalation of iodine anions is possible to tune the band structure of $Bi_2O_2CO_3$. Such anion intercalation strategy has been regarded as a promising way to develop novel photocatalysts, such as $Bi_2O(OH)_2SO_4$ [16].

Some BOB compounds, like δ-Bi_2O_3, have the potential to incorporate iodine anions and transform into iodine containing BOB compounds, which is represented by the technology to capture and store radioactive iodine in nuclear waste [17–19]. On the other hand, upon calcinations the bounded iodine anions in the lattice of bismuth oxyiodide tend to diffuse out and produce a series of nonstoichiometric $Bi_2O_{3-x}I_{2x}$ compounds with defects [1]. Generally, the decrease of iodine in bismuth oxyiodides would result in the downward shift of valence band potentials and the increase of oxidation ability of photogenerated holes, while also enlarge band gaps and decrease the ranges of responsive light [1,4]. Among bismuth oxyiodides, $Bi_7O_9I_3$ and $Bi_4O_5I_2$ display the highest photocatalytic activity [4]. However, there is a great potential to further optimized x value to balance the oxidation power and optical absorption, but a strategy is demanded to realize it before the production of Bi_5O_7I.

Fabricating semiconductor heterostructures is an important way to develop photocatalysts with minimized weakness and

* Corresponding author. Fax: +86 21 54740825.
E-mail address: long_mc@sjtu.edu.cn (M. Long).

http://dx.doi.org/10.1016/j.apcatb.2015.11.025
0926-3373/

maxiumized strength [20–27]. Comprising of hetero components with matchable band potentials but random contact forms show improved photogenerated charge separation, such as β-Bi_2O_3/$Bi_2O_2CO_3$ [23], $Bi_2O_2CO_3$/BiOI [24]. Moreover, confining the intrinsically unstable material with a layer of hetero compound is an effective strategy to enhance the stability [28]. Herein, according to the interaction between inner bismuth oxyiodide and surface carbonate at elevated temperatures, a heterostructure of nonstoichiometric $Bi_2O_{3-x}I_{2x}$ covered with iodine intercalated $Bi_2O_2CO_3$ was developed through a treatment of $Bi_7O_9I_3$ in urea solution and subsequent calcinations. Benefiting from the unique structural feature and the proper iodine content in $Bi_2O_{3-x}I_{2x}$, the synthesized heterostructure exhibits significantly enhanced photocatalytic activity and stability in organic degradation.

2. Experimental

2.1. Sample synthesis

$Bi_7O_9I_3$ was synthesized by a solvothermal method [1–3]. Briefly, 2.5 mmol bismuth nitrate dissolved in 24 mL ethylene glycol, then an equal amount of KI was added into the mixture. The final solution was sealed in a 30 mL Teflon-lined stainless steel autoclave and maintained at 160 °C for 12 h. The final orange powder was filtrated, washed with de-ionized water repeatedly and then dried in an oven. As prepared $Bi_7O_9I_3$ was performed an in situ transformation by introducing $Bi_7O_9I_3$ powder into a 0.2 M urea solution and stirring at 90 °C for different durations. The obtained products were dried and assigned as BCOI-*t* (*t* is the treating time). BCOI-*t* precursors were calcined by ramping to temperature *T* at a rate of 1 °C/min and holding for 2 h. The resulting products were assigned as BCOI-*t*-*T*. The untreated $Bi_7O_9I_3$ and the calcined $Bi_7O_9I_3$ at 350 °C (assigned as $Bi_7O_9I_3$-350) were used as control samples. Moreover, $Bi_2O_2CO_3$ was synthesized for comparisons through a precipitation method [24]. Briefly, 2.425 g bismuth nitrate was dissolved in a 5 mL nitric acid aqueous solution (1 M) to obtain the solution A, and 0.25 g cetyltrimethyl ammonium bromide (CTAB) and 40 mmol sodium carbonate were dissolved in 70 mL water to obtain the solution B. Solution A was dropwise added into solution B to obtain the precipitation, which was filtered, washed and dried at 80 °C for 4 h.

2.2. Characterizations

Ratios of Bi to I were calculated from the data of elemental analyses, which were collected on an X-ray fluorescence analyzer (XRF-1800, Shimadzu). The thermal stability was investigated by a thermogravimetric-differential thermal analyzer (TG-DTA, TGA/DSC 1, Mettler Toledo) in an air atmosphere at a flow rate of 50 mL/min. The heating program was set as: ramping at 5 °C/min to 200 °C, 350 °C, 400 °C and 450 °C continuously, and holding at each point for 30 min; finally ramping to 600 °C at the same rate. The crystal phases of catalysts were analyzed using powder X-ray diffraction (XRD, D/max-2200, Rigaku Corp.) with Cu Kα radiation, operating at 40 kV 30 mA (λ = 0.154 nm). Diffuse reflectance spectra (DRS) were recorded on a Lambda 950 UV/vis spectrophotometer (PerkinElmer Instrument Co., Ltd.), and the reflectance was converted into absorption by the Kubelka–Munk method. X-ray photoelectron spectroscopy (XPS) measurements were performed on a Kratos AXIS Ultra DLD instrument with the monochromatic Al Kα radiation ($h\nu$ = 1486.6 eV). A high resolution transmission electron microscope (HRTEM, JEM-2100F, JEOL, Japan) was used to observe the morphology of catalysts.

2.3. Photoelectrochemical and photocatalytic tests

Photoelectrodes were prepared by coating the pastes of BCOI-1-350 or $Bi_7O_9I_3$-350 onto a slice of FTO glass through the doctor blade method [29,30]. The photoelectrochemical test system was composed of a CHI 606E Potentiostat/Galvanostat, a 500 W xenon lamp, and a homemade three-electrode cell. The as prepared photoelectrode, a platinum wire and a Ag/AgCl electrode were used as the working, counter and reference electrodes, respectively. The exposed area of the photoelectrodes under illumination was 0.785 cm^2. The electrolyte solution was a 0.5 M Na_2SO_4 aqueous solution, which was bubbled with N_2 gas for 30 min before tests. A 420 nm cutoff filter was utilized in specific conditions. The photocurrent transients were taken at a bias of +0.2 V vs. Ag/AgCl.

The photocatalytic activity was evaluated by phenol degradation under visible light from a 1000 W xenon lamp with a cutoff filter (λ > 400 nm). In a typical test, 0.05 g catalyst was added into a 50 mL phenol solution (initial concentration 10 mg/L). The suspension was stirred in the dark for 15 min to reach adsorption equilibrium before being exposed to visible light irradiation. During irradiation, the samples were taken at regular time intervals, filtered, and then monitored using a colorimeter on a UNICO UV-2102 spectrometer.

2.4. Theoretic calculations

First-principles calculations were performed by density functional theory (DFT) method using a plane-wave basis set, and implemented using Quantum ESPRESSO [31]. The generalized gradient approximation (GGA) with Perdew–Burke–Ernzerhof (PBE) exchange–correlation functional, and norm-conserving pseudopotentials are used for all calculations. Wave functions were expanded in plane-waves with a kinetic energy cutoff of 80 Ry and 320 Ry for the smooth and augmented part of density, respectively. Orthorhombic $Bi_2O_2CO_3$ (a = 3.865; b = 3.862; c = 13.675; $\alpha = \beta = \gamma = 90°$) and their corresponding compounds with iodine substitute for carbonate (the ratio of Bi/I is 64 or 32) were modeled and calculated. Calculations were carried out on $2 \times 1 \times 2$ supercells at the Γ point of the Brillouin zone for the calculations of iodine containing cases. The Broyden–Fletcher–Goldfarb–Shanno (BFGS) geometry optimization scheme was performed until forces and total electron energy converged below 0.005 eV $Å^{-1}$ and 10^{-5} Ry, respectively.

3. Results and discussion

3.1. Characterizations of BCOI-t

Microsphere nanocrystal $Bi_7O_9I_3$ was synthesized by ethylene glycol solvothermal method, whose Bi/I ratio was determined as 2.36 by XRF analyzer, and whose characteristic peak at 28.9° was quite different from the (1 0 2) plane of tetragonal phase BiOI (JCPDS 10-0445) at 29.7° (Fig. 1) [32]. Subsequently, $Bi_7O_9I_3$ powder was stirred in a urea solution at 90 °C. The hot urea solution is known

Table 1
Bismuth and iodine molecular ratios and $Bi_7O_9I_3$ percentages.

Catalysts	$Bi_7O_9I_3$	BCOI-05	BCOI-1	BCOI-2	BCOI-4	$Bi_7O_9I_3$-350	BCOI-1-350	BCOI-2-350
Molecular ratio (Bi/I)	2.36	3.81	4.60	7.08	21.32	2.80	5.14	6.95
$Bi_7O_9I_3$ molecular percentage (%)	100	31.1	22.7	12.3	3.4	–	–	–

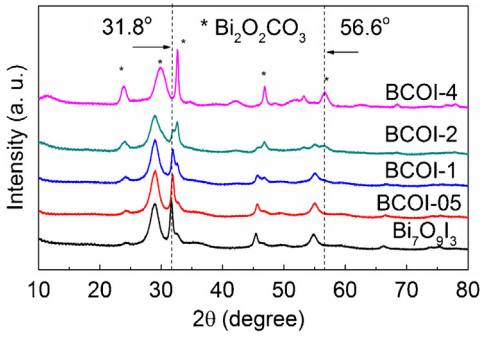

Fig. 1. XRD patterns of treated (BCOI-t) and the untreated $Bi_7O_9I_3$.

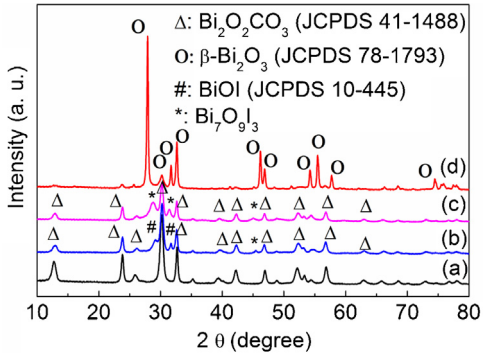

Fig. 2. XRD patterns of (a) $Bi_2O_2CO_3$ and (b–d) those calcined at 350 °C: $Bi_2O_2CO_3$ with (b) I_2 (30 wt%); (c) $Bi_7O_9I_3$ (50 wt%) or (d) without additive.

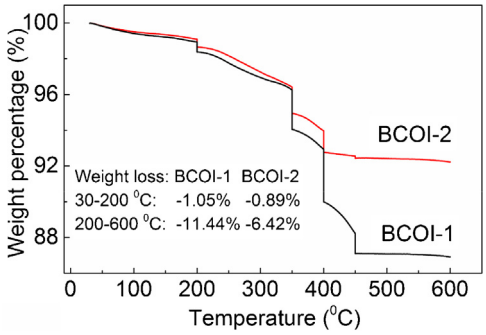

Fig. 3. Thermogravimetric (TG) curves of BCOI-1 and BCOI-2.

as the homogenous precipitation method and usually employed for immobilizing Au nanoparticles on the surface of oxides [33,34]. With the gradual release of carbonates and the slow increase of pH, $Bi_7O_9I_3$ transforms into bismuth oxide or bismuth oxide carbonate with different percentages, which depend on the treatment time, as described by Eqs. (1) and (2), respectively. The as-prepared powder is assigned as BCOI-*t* (*t* is the treatment time). The ratios of elementary Bi and I are shown in Table 1, which increase from the initial 2.36 to as high as 21.32 after 4 h treatment. Regardless of the products as $Bi_2O_2CO_3$ or Bi_2O_3, the molecular percentages of residual $Bi_7O_9I_3$ are the same (Table 1). According to the Bi/I ratio of 3.81 for BCOI-05, about 68.9% $Bi_7O_9I_3$ disappears after only 0.5 h treatment, suggesting that the conversion of bismuth oxyiodides in such a condition is facile and fast. Due to the comparable molecular masses of bismuth oxides and carbonate, the weight percentage of $Bi_7O_9I_3$ in BCOI-*t* varies in a narrow ranges. For example, there are about 53–56 wt% and 35–37 wt% $Bi_7O_9I_3$ in BCOI-1 and BCOI-2, respectively. According to the XRD patterns in Fig. 1, the characteristic peak at 31.8° for BCOI-4 has almost disappeared, indicating the conversion of $Bi_7O_9I_3$ approaches complete after extending treatment. Moreover, the emerged new peaks in the pattern can be assigned to the characteristic planes of $Bi_2O_2CO_3$ (JCPDS 41-1488), suggesting that $Bi_2O_2CO_3$ is the major final product in the hot urea solution [23]. It can be understood that the produced oxides incline to convert into $Bi_2O_2CO_3$ at such a condition.

$$2Bi_7O_9I_3 + 6CO_3^{2-} \rightarrow 7Bi_2O_3 + 6I^- + 6CO_2 \quad (1)$$

$$2Bi_7O_9I_3 + 7CO_3^{2-} + 4H_2O \rightarrow 7Bi_2O_2CO_3 + 6I^- + 8OH^- \quad (2)$$

$$Bi_2O_2CO_3 \xrightarrow{\Delta} \beta - Bi_2O_3 + CO_2 \quad (3)$$

3.2. *Changes of BCOI-*t *under calcinations*

Both bismuth oxyiodide and $Bi_2O_2CO_3$ are thermally unstable. $Bi_2O_2CO_3$ starts decomposing at about 330 °C and almost completely converts into tetragonal β-Bi_2O_3 at 400 °C (Fig. S2) [13,35]. Simultanously, calcinations would induce the continuous escape of iodine from the lattice of $Bi_7O_9I_3$, while its phase transition could not be observed below 350 °C [1]. If there was only decomposition of $Bi_2O_2CO_3$ but no change of $Bi_7O_9I_3$, the theoretical ratio of Bi/I should not change. However, the ratio of BCOI-1 increases from 4.61 to 5.14 after calcined at 350 °C, indicating the loss of iodine during calcinations. It should be noted that the reduction percentage of iodine is less than the untreated $Bi_7O_9I_3$ [1]. It is interesting that there is nearly no loss of iodine for BCOI-2, as the ratio changes from 7.08 to 6.95 for BCOI-2-350 (Table 1). The dramatically suppressed iodine loss can be ascribed to the block or trap of diffused iodine by the surface species, as the intercalation of iodine into the layered BOB compounds has been widely observed [17–19].

On the other hand, it was found that the thermal decomposition of $Bi_2O_2CO_3$ at 350 °C was dramatically inhibited by iodine intercalations, which was proved by XRD patterns in Fig. 2. $Bi_2O_2CO_3$ was calcined at 350 °C for 2 h at a ramp rate of 1 °C/min, and the XRD pattern of the resulted yellow powder (curve d) was mainly in accordance with tetragonal β-Bi_2O_3 (JCPDS 78-1793). However, when mixing $Bi_2O_2CO_3$ with $Bi_7O_9I_3$ or I_2, the decomposition of $Bi_2O_2CO_3$ was significantly inhibited, as there is no observable change in both the appearance of powder and their XRD patterns. The indications of β-Bi_2O_3 in their XRD patterns are negligible. Such inhibited decomposition of $Bi_2O_2CO_3$ could be ascribed to the intercalation of iodine into the layer of $[Bi_2O_2]^{2+}$ slabs.

Thermogravimetric (TG) curves of BCOI-1 and BCOI-2 were measured to understand the changes of BCOI-*t* during calcinations (Fig. 3). The temperature program is: ramping at 5 °C/min to 200, 350, 400 and 450 °C, holding at each point for 30 min; and finally terminating at 600 °C. The weight losses of BCOI-*t* below 200 °C are mainly attributed to the evaporation of bounded water, while those in the range of 200–600 °C are ascribed to the transition of $Bi_7O_9I_3$ and the completely decomposition of $Bi_2O_2CO_3$. It should be noted that the decomposition of $Bi_2O_2CO_3$ in BCOI-*t* will not be inhibited when calcined at as high as 600 °C. Theoretically, the weight losses are 9.57 wt% and 28.21 wt% for the transformation of $Bi_7O_9I_3$ into Bi_5O_7I and Bi_2O_3, respectively, and 8.63 wt% for the decomposition of $Bi_2O_2CO_3$. Both Bi_5O_7I and Bi_2O_3 could be the stable compounds at 600 °C. According to TG curves, the total weight losses above 200 °C are measured as 11.44 wt% and 6.42 wt% for BCOI-1 and BCOI-2, respectively. The measured weight loss for BCOI-2 is even less than all theoretic data for both the transition of $Bi_7O_9I_3$ and decomposition of $Bi_2O_2CO_3$, suggesting that BCOI-2 is a mixture of $Bi_2O_2CO_3$, $Bi_7O_9I_3$ and Bi_2O_3, among which the last one do not lose weight below 600 °C.

As measured in our previous work [1], the total weight loss for untreated $Bi_7O_9I_3$ in the same stages is 17.22 wt%, suggesting that $Bi_7O_9I_3$ transform into a mixture of Bi_5O_7I and Bi_2O_3. According to this value and the median value of $Bi_7O_9I_3$ in BCOI-1 (54.5 wt%), the weight loss coming from $Bi_7O_9I_3$ is estimated as

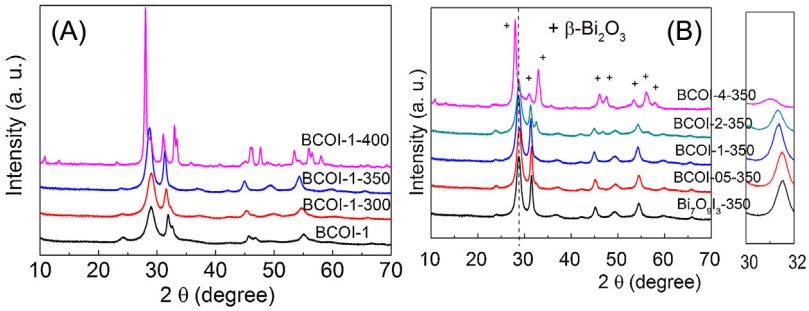

Fig. 4. XRD patterns of various catalysts: (A) BCOI-1-T; (B) BCOI-t-350 and $Bi_7O_9I_3$-350.

9.38 wt%. Considering 11.44 wt% weight loss of BCOI-1, the contribution from $Bi_2O_2CO_3$ decomposition is about 2.06 wt%, and then the weight percentage of $Bi_2O_2CO_3$ is calulated as 23.8 wt% according to the theoretic value of its decomposition. Thus, about 21.7 wt% of BCOI-1 is attributed to the substance that do not lose weight after calcination, like Bi_2O_3. According to above analyses, the presence of oxides in BCOI-*t* is possible. The unobservable indications of bismuth oxides in the XRD patterns of BCOI-*t* could be attributed to the homogeneously dispersion and the low molecular percentages.

3.3. *Characterizations of BCOI*-t-T

Fig. 4A is the XRD patterns of calcined BCOI-1 at various temperatures, while Fig. 4B is those for different BCOI-*t* precursors calcined at 350 °C. The characteristic peaks for (0 0 2) and (2 2 0) planes of β-Bi_2O_3 at 31.8° and 32.6° are coincident with those (1 1 0) planes of $Bi_7O_9I_3$ and $Bi_2O_2CO_3$, respectively [2,23]. Thus the peak at 27.9° for (2 0 1) plane of β-Bi_2O_3 can be used as the indication of its existance. When BCOI-1 was calcined at 300 or 350 °C, the characteristic peaks in the XRD patterns display increased intensities with only slightly downward shift of the peaks at 28.9° and 31.8° to 28.6° and 31.4°, respectively. No appearance of β-Bi_2O_3 can be observed after calcinations. However, elevating the calcination temperature to 400 °C, BCOI-1 shows obvious transition, and the emergance of Bi_5O_7I (JCPDS 40-0548) can be discerned in the XRD pattern, which is the same as the untreated $Bi_7O_9I_3$ [1].

On the other hand, the characteristic peak at 27.9° for β-Bi_2O_3 can only be observed in the XRD pattern of BCOI-4-350 (Fig. 4B), accompanying with other characteristic peaks of β-Bi_2O_3. This can be attributed to the negligible inhibition on $Bi_2O_2CO_3$ decomposition due to the low percentage of $Bi_7O_9I_3$ and high content of $Bi_2O_2CO_3$ in BCOI-4. The presence of β-Bi_2O_3 is undesirable due to its poor stability in photocatalytic applications. As we can observe, the characteristic peak of $Bi_7O_9I_3$-350 at about 31.54° downward shifts slightly to 31.50°, 31.37° and 31.33° for the samples of BCOI-05-350, BCOI-1-350 and BCOI-2-350, respectively, indicating a continuous change of nonstoichiometric bismuth oxyiodide compositions. Simultaneously, a decreased intensity of peak at 32.6° for $Bi_2O_2CO_3$ can be observed. The undiscernible indication of β-Bi_2O_3 or other polymorph Bi_2O_3 suggests that the produced oxides could be involved in the formation of nonstoichiometric bismuth oxyiodide, or the intercalation of iodine could increase the lattice disorder of $Bi_2O_2CO_3$ and result in the decreased diffraction signals. We can assume the formula of the nonstoichiometric bismuth oxyiodide in BCOI-*t*-350 is $Bi_2O_{3-x}I_{2x}$, wherein the oxidation potential of the valance holes depends much on the *x* values.

The intercalation of iodine in $Bi_2O_2CO_3$ can be further proved by the high resolution XPS spectra of I 3d (Fig. 5A). Before calcination, the doublet of I 3d spectrum centering at 619.0 and 630.5 eV correspond to I $3d_{5/2}$ and I $3d_{3/2}$ in $Bi_2O_{3-x}I_{2x}$, respectively [36]. The spectrum for BCOI-1 cannot be deconvoluted into any other doublet. However, after calcination, the spectrum of I_{3d} for BCOI-1-350 can be deconvoluted into two doublets. The new doublet at the higher binding energies can be ascribed to the intercalated iodine in the layered lattice of $Bi_2O_2CO_3$ [37], which is close to the neutral iodine (I_2, ~620 eV). According to the ratios of integral areas, the molecular percentage of the intercalated iodine is estimated about 5.8 wt%. Considering 23.8 wt% surface covered $Bi_2O_2CO_3$ in BCOI-1 and the Bi/I ratio of 5.14 for BCOI-1-350, overlooking the decomposition of $Bi_2O_2CO_3$, and excluding the intercalated iodine, we can estimated an *x* value as about 0.243. It should be noted that even if there is a partial decomposition of $Bi_2O_2CO_3$ and the involvement of the produced oxides in the formation of $Bi_2O_{3-x}I_{2x}$, the changes of *x* value is quite low. Thus, the composition of BCOI-1-350 can be roughly determined as a composite of $Bi_2O_{3-x}I_{2x}$ ($x = 0.243$)/$Bi_2O_2CO_3$(I), a nonstoichiometric compound $Bi_2O_{3-x}I_{2x}$ covered by iodine intercalated $Bi_2O_2CO_3$.

Table 2
Estimated band-gap energy (E_g), valence band edge potentials (E_{VB}) and conduction band edge potentials (E_{CB}) of as synthesized catalysts.

Catalyst	$Bi_7O_9I_3$	BCOI-1	$Bi_7O_9I_3$-350	BCOI-1-350
E_g (eV)	2.04	2.11	2.31	2.43
E_{CB} (eV)	−0.63 [1]	–	−0.48 [1]	−0.44
E_{VB} (eV)	1.41 [1]	–	1.83 [1]	1.99

Fig. 5B is the DRS spectra of several comparison catalysts, and Table 2 shows the estimated band-gap energy (E_g), valence band edge potentials (E_{VB}) and conduction band edge potentials (E_{CB}) as synthesized catalysts. The apparent band gap of BCOI-1-350 is estimated as 2.43 eV, slightly larger than the band gap of $Bi_7O_9I_3$-350 (~2.31 eV). Simultaneously, the valence band of BCOI-1-350 was determined as 1.99 V by the slurry method (Fig. S3). It is also more anodic than that of $Bi_7O_9I_3$-350 (~1.83 V) [1]. According to the Bi/I ratio of 2.80 for $Bi_7O_9I_3$-350, *x* value in the formula of $Bi_2O_{3-x}I_{2x}$ for $Bi_7O_9I_3$-350 can be calculated as 0.357. Comparing with $Bi_7O_9I_3$-350, the lower iodine content in BCOI-1-350 ($x = 0.243$) induces a slightly enlarged band gap and a more anodic potential of valence band positions, indicating that photogenerated holes possess a stronger oxidation ability.

BCOI-1-350 has kept the microsphere structure as its precursor $Bi_7O_9I_3$. According to the HRTEM images in Fig. 5C, two distinct regions with different parallel fringes can be identified. The distance between the adjacent fringes in the outlayer region is about 0.664 nm, corresponding to the interplaner space of $Bi_2O_2CO_3$ (0 0 2). The thickness of this region is about 3–5 nm. The smaller distance in the inner layer is about 0.311 nm, which can be ascribed to a crystal facet of $Bi_2O_{3-x}I_{2x}$ that corresponds to the strong diffraction peak at 28.7°.

To understand the electronic structure of iodine intercalated $Bi_2O_2CO_3$, a DFT calculation was taken for $Bi_2O_2CO_3$ and iodine intercalated $Bi_2O_2CO_3$ with the Bi/I ratios of 64 and 32, corre-

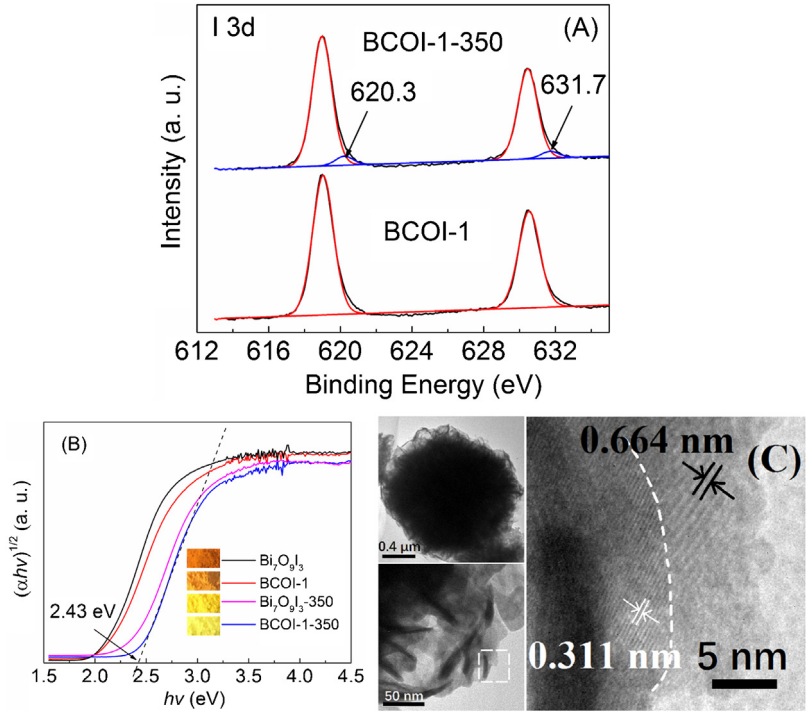

Fig. 5. (A) XPS spectra of I 3d for BCOI-1 and BCOI-1-350; (B) DRS spectra of different catalysts; (C) HRTEM images of BCOI-1-350.

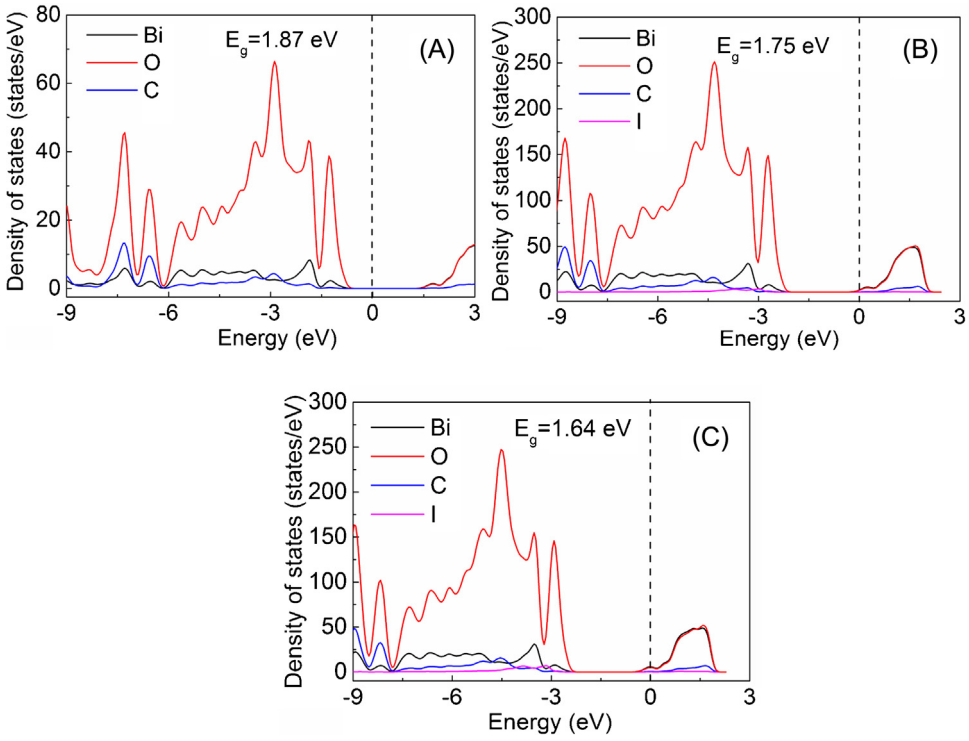

Fig. 6. Calculated partial density of states (PDOS) for $Bi_2O_2CO_3$ (A) and iodine intercalated $Bi_2O_2CO_3$ with different iodine contents: (B) Bi/I = 64; (C): Bi/I = 32.

sponding to the atomic percentages of iodine are 0.4% and 0.8%, respectively. The calculated partial density of states (PDOS) are shown in Fig. 6. It shows that orbitals from iodine involve in the composition of valence band. Moreover, the band gaps of iodine intercalated $Bi_2O_2CO_3$ narrow from 1.87 eV to 1.75 and 1.64 eV with the increases of iodine contents to 0.4% and 0.8%, respectively, suggesting that the intercalation of iodine would decrease the band gap of $Bi_2O_2CO_3$. Therefore iodine intercalated $Bi_2O_2CO_3$ in BCOI-1-350 could possess a visible light activity due to the theoretically narrowed band gap. Moreover, it is interesting that the band positions shift downwards with the increases of intercalated iodine, indicating a higher oxidizing power of photogenerated holes on the valence band [1,38]. Both of the narrowed band gaps and shift band positions are favorable for the visible light photooxidation reaction of this catalyst.

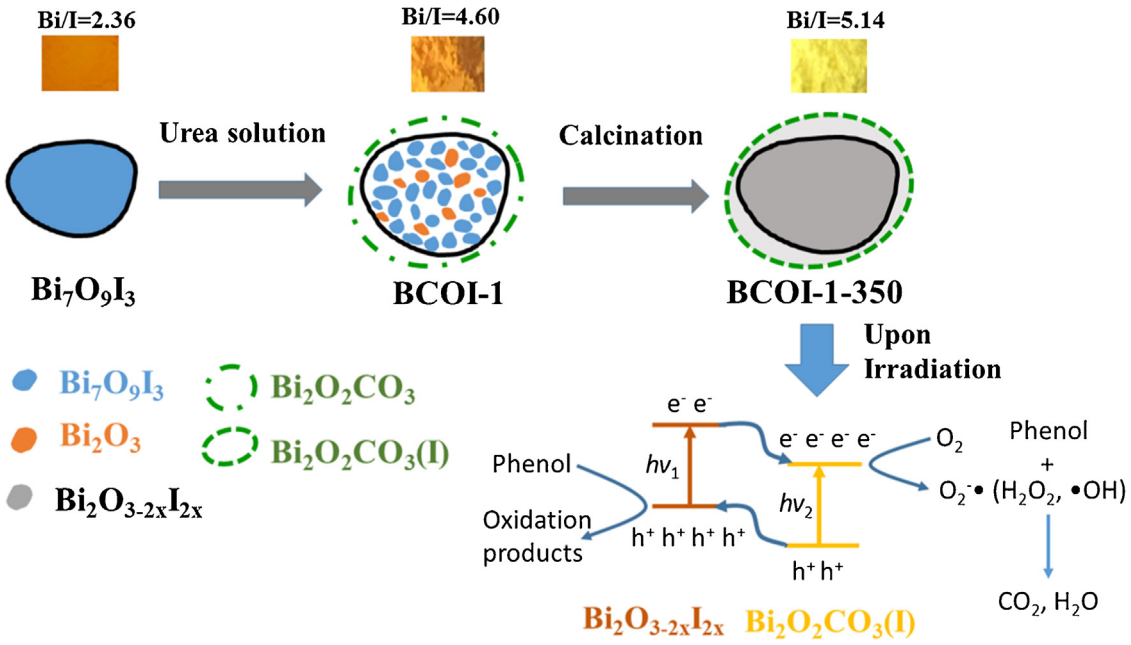

Scheme 1. A scheme for the formation of heterostructure BCOI-1-350 and the mechanism on phenol photocatalytic degradation.

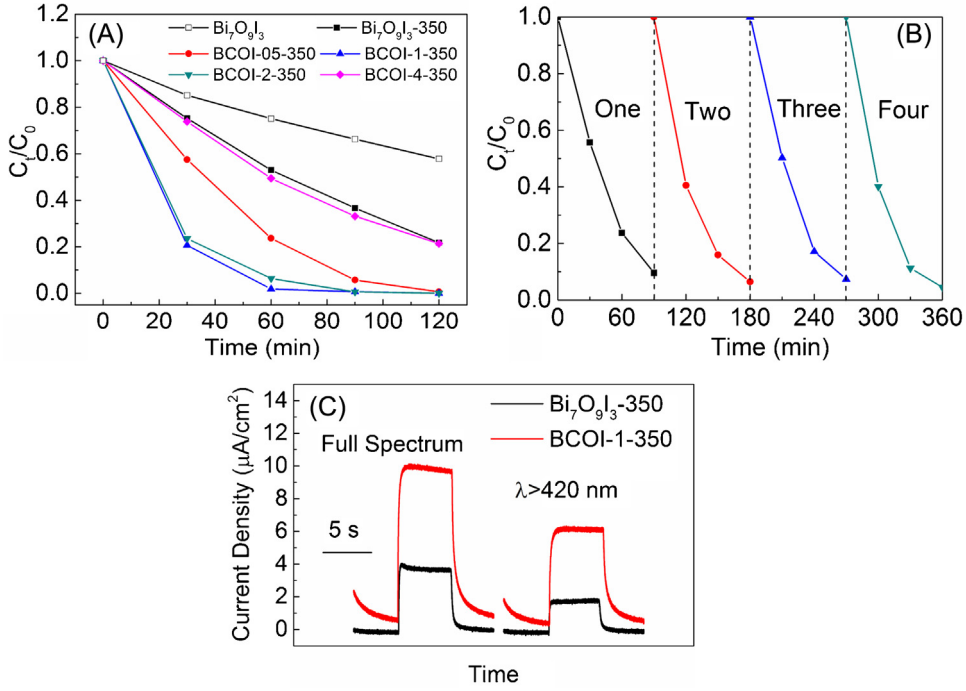

Fig. 7. (A) Photocatalytic degradation of phenol in the presence of different photocatalysts under visible light irradiation (λ > 400 nm); (B) four cycles of visible light photocatalytic degradation of phenol using BCOI-1-350; (C) photocurrents of $Bi_7O_9I_3$-350 and BCOI-1-350 under different illumination conditions (+0.2 V vs. Ag/AgCl).

3.4. *Performance of BCOI*-t-T

Significantly improved visible light photocatalytic and photoelectrochemical performance were observed for the calcined catalysts (Fig. 7). BCOI-1-350 exhibits the highest photooxidation activity for phenol degradation (Fig. 7A). Phenol reduction is more than 80% after only 30 min irradiation. Initial apparent first-order reaction rate constants were calculated by fitting the photocatalytic degradation data in the first 60 min. The reaction rate constant in the presence of BCOI-1-350 (0.0666 min^{-1}) is more than 4 times of the untreated $Bi_7O_9I_3$-350 (0.0126 min^{-1}), and more than 15 times of $Bi_7O_9I_3$ (0.0044 min^{-1}). With the covered iodine intercalated $Bi_2O_2CO_3$, the photocatalyst BCOI-1-350 is also stable after repeated tests (Fig. 7B). Furthermore, photocurrents generated from $Bi_7O_9I_3$-350 and BCOI-1-350 are compared in (Fig. 7C). The photocurrents from BCOI-1-350 electrode are about 2.45 and 3.16 times of those from $Bi_7O_9I_3$-350 under full spectrum and λ > 420 nm irradiation, respectively.

3.5. Mechanism

The foramtion chemistry of this unique heterostructure of BCOI-1-350 can be understood from Scheme 1. Under the gradually increased pH and the released carbonates in hot urea solution, outlayer of $Bi_7O_9I_3$ would partially converts into $Bi_2O_2CO_3$, as well as Bi_2O_3. After extending reaction, Bi_2O_3 would also incline to convert into $Bi_2O_2CO_3$, which is the final products in such a condition. The compositions of the products are tailored by the treating time. In fact, the visible light photocatalytic activities of the heterostructure BCOI-*t* are poor (Fig. S1), because of the covered wide band gap $Bi_2O_2CO_3$. It is interesting that there is a special interaction between inner layer of $Bi_7O_9I_3$ and outlayer of $Bi_2O_2CO_3$ during calcinations below 400 °C, and this interaction is a combination of the suppressed iodine diffusion and loss, the intercalation of iodine into $Bi_2O_2CO_3$, and the inhibited thermal decomposition of $Bi_2O_2CO_3$. The combination of the iodine loss in urea solution and the suppressed iodine loss during calcinations is favorable to retain a controllable iodine content in the nonstoichiometric bismuth oxyiodide before the emergance of Bi_5O_7I, while the intercalation of iodine leads to a decrease band gap of $Bi_2O_2CO_3$. The lower iodine content in $Bi_2O_{3-x}I_{2x}$ contributes to a higher oxidation potential of photogenerated holes, simultaneously the covered iodine intercalated $Bi_2O_2CO_3$ would retard the transformation of bismuth oxyiodide. Therefore, a unique heterostructure of nonstoichiometric bismuth oxyiodide and iodine intercalated $Bi_2O_2CO_3$, like BCOI-1-350, can be fabricated from the precursor $Bi_7O_9I_3$ (Scheme 1). Although we cannot synthesize the individual component in BCOI-1-350 for more detailed investigations, the visible light responsive outlayer of iodine intercalated $Bi_2O_2CO_3$ can be expected according to the theoretic calculation, the apparent DRS spectrum and significantly enhanced visible light photocatalytic activity.

The heterojunction in the composite BCOI-1-350, as well as the mechansim on phenol degradation is plotted in Scheme 1. The bias between the two components, nonstoichiometric bismuth oxyiodide ($Bi_2O_{3-x}I_{2x}$) and iodine intercalated $Bi_2O_2CO_3$ ($Bi_2O_2CO_3$(I)), promotes charge separation and delocalization on the individual component. Simultaneously, photogenerated electrons on the conduction bands can be scavenged by oxygen and transformed into active $O_2^{-\bullet}$. The valence band potential of $Bi_2O_{3-x}I_{2x}$ is almost high enough to produce $^\bullet$OH ($^\bullet$OH/OH$^-$ = +1.99 V), and the other pathway from $O_2^{-\bullet}$ radicals and electrons could also produce $^\bullet$OH, as shown in Eqs. (4) and (5) [39,40]. Therefore, the enhanced photocatalytic performance of BCOI-1-350 should be attributed to the promoted charge separation under the bias of different band potentials of hetero components, the stronger oxidation power of photogenerated holes, the produced radicals of $^\bullet$OH and $O_2^{-\bullet}$, as well as the inhibited transformation of the inner layer bismuth oxyiodide under the protection of the surface covered iodine intercalated $Bi_2O_2CO_3$.

$$O_2^{\bullet-} + O_2^{\bullet-} + 2H^+ \rightarrow H_2O_2 + O_2 \quad (4)$$

$$H_2O_2 + e^- \rightarrow {}^\bullet OH + OH^- \quad (5)$$

4. Conclusions

We have described an efficient and stable visible light BOB photocatalyst with a unique heterostructure, a nonstoichiometric bismuth oxyiodide $Bi_2O_{3-x}I_{2x}$ covered by iodine intercalated $Bi_2O_2CO_3$. A low iodine content can be achieved before the production of Bi_5O_7I, which contributes to high oxidation potential of photogenerated holes. The covered iodine intercalated $Bi_2O_2CO_3$ protects inner bismuth oxyiodide from transformation. The systhesis of this heterostructure is realized through a treatment of $Bi_7O_9I_3$ in a urea solution and subsequent calcinations. Those effects of blocked iodine diffusion and inhibited decomposition of $Bi_2O_2CO_3$ through the iodine intercalation represent new strategies to tune the iodine content in bismuth oxyiodide compounds, and to fabricate novel delicate BOB photocatalytic heterostructures for environmental applications.

Acknowledgements

Authors acknowledge financial supports from the Natural Science Foundation of China (21377084), Shanghai Municipal Natural Science Foundation (13ZR1421000) and Special Fund for Agro-scientific Research in the Public Interest (201503107). We also acknowledge the Center for High Performance Computing at Shanghai Jiao Tong University for providing computing resources on the Π supercomputer.

Appendix A. Supplementary data

Supplementary data associated with this article can be found, in the online version, at http://dx.doi.org/10.1016/j.apcatb.2015.11.025.

References

[1] M. Long, P. Hu, H. Wu, Y. Chen, B. Tan, W. Cai, J. Mater. Chem. A 3 (2015) 5592–5598.
[2] Q.C. Liu, D.K. Ma, Y.Y. Hu, Y.W. Zeng, S.M. Huang, ACS Appl. Mater. Interfaces 5 (2013) 11927–11934.
[3] X. Zhang, Z.H. Ai, F.L. Jia, L.Z. Zhang, J. Phys. Chem. C 112 (2008) 747–753.
[4] X. Xiao, C. Liu, R. Hu, X. Zuo, J. Nan, L. Li, L. Wang, J. Mater. Chem. 22 (2012) 22840.
[5] S. Sun, W. Wang, L. Zhang, L. Zhou, W. Yin, M. Shang, Environ. Sci. Technol. 43 (2009) 2005–2010.
[6] L.S. Zhang, W.Z. Wang, J. Yang, Z. Chen, W. Zhang, L. Zhou, S. Liu, Appl. Catal. A Gen. 308 (2006) 105–110.
[7] J. Eberl, H. Kisch, Photochem. Photobiol. Sci. 7 (2008) 1400–1406.
[8] Y. Sun, W. Wang, L. Zhang, Z. Zhang, Chem. Eng. J. 211–212 (2012) 161–167.
[9] P. Riente, A. Matas Adams, J. Albero, E. Palomares, M.A. Pericas, Angew. Chem. Int. Ed. 53 (2014) 9613–9616.
[10] H.Y. Jiang, P. Li, G. Liu, J. Ye, J. Lin, J. Mater. Chem. A 3 (2015) 5119–5125.
[11] L. Zhou, W. Wang, H. Xu, S. Sun, M. Shang, Chem. Eur. J. 15 (2009) 1776–1782.
[12] M. Schlesinger, M. Weber, S. Schulze, M. Hietschold, M. Mehring, Chem. Open 2 (2013) 146–155.
[13] P. Taylor, S. Sunder, V.J. Lopata, Can. J. Chem. 62 (1984) 2863–2873.
[14] S. Iyyapushpam, S.T. Nishanthi, D.P. Padiyan, J. Phys. Chem. Solids 81 (2015) 74–78.
[15] Y. Zheng, F. Duan, M. Chen, Y. Xie, J. Mol. Catal. A Chem. 317 (2010) 34–40.
[16] H. Tian, F. Teng, J. Xu, S. Lou, N. Li, Y. Zhao, M. Chen, Sci. Rep. 5 (2015) 7770.
[17] L. Liu, W. Liu, X. Zhao, D. Chen, R. Cai, W. Yang, S. Komarneni, D. Yang, ACS Appl. Mater. Interfaces 6 (2014) 16082–16090.
[18] D.P. Scarfe, S. Bhavaraju, A.J. Jacobson, Chem. Commun. (1997) 313–314.
[19] J.L. Krumhansl, T.M. Nenoff, Appl. Geochem. 26 (2011) 57–64.
[20] X. Gao, H.B. Wu, L. Zheng, Y. Zhong, Y. Hu, X.W. Lou, Angew. Chem. Int. Ed. 53 (2014) 5917–5921.
[21] G. Manna, R. Bose, N. Pradhan, Angew. Chem. Int. Ed. 53 (2014) 6743–6746.
[22] P. Madhusudan, J. Ran, J. Zhang, J. Yu, G. Liu, Appl. Catal. B Environ. 110 (2011) 286–295.
[23] R. Hu, X. Xiao, S. Tu, X. Zuo, J. Nan, Appl. Catal. B Environ. 163 (2015) 510–519.
[24] L. Chen, S.F. Yin, S.L. Luo, R. Huang, Q. Zhang, T. Hong, P.C.T. Au, Ind. Eng. Chem. Res. 51 (2012) 6760–6768.
[25] D. Yue, D.M. Chen, Z.H. Wang, H. Ding, R.L. Zong, Y.F. Zhu, Phys. Chem. Chem. Phys. 16 (2014) 26314–26321.
[26] D. Chen, Z. Kuang, Q. Zhu, Y. Du, H. Zhu, Mater. Res. Bull. 66 (2015) 262–267.
[27] A. Hameed, M. Aslam, I.M.I. Ismail, N. Salah, P. Fornasiero, Appl. Catal. B Environ. 163 (2015) 444–451.
[28] S. Sanna, V. Esposito, J.W. Andreasen, J. Hjelm, W. Zhang, T. Kasama, S.B. Simonsen, M. Christensen, S. Linderoth, N. Pryds, Nat. Mater. 14 (2015) 500–504.
[29] S. Suzuki, K. Itoh, M. Ohgaki, M. Ohtani, M. Ozawa, Ceram. Int. 25 (1999) 287–291.
[30] J. Jiang, M. Long, D. Wu, W. Cai, J. Mol. Catal. A Chem. 335 (2011) 97–104.
[31] P. Giannozzi, S. Baroni, N. Bonini, M. Calandra, R. Car, C. Cavazzoni, D. Ceresoli, G.L. Chiarotti, M. Cococcioni, I. Dabo, A. Dal Corso, S. de Gironcoli, S. Fabris, G. Fratesi, R. Gebauer, U. Gerstmann, C. Gougoussis, A. Kokalj, M. Lazzeri, L. Martin-Samos, N. Marzari, F. Mauri, R. Mazzarello, S. Paolini, A. Pasquarello, L. Paulatto, C. Sbraccia, S. Scandolo, G. Sclauzero, A.P. Seitsonen, A. Smogunov, P. Umari, R.M. Wentzcovitch, J. Phys. Condens. Matter 21 (2009) 395502.

[32] W. Wang, F. Huang, X. Lin, Scripta Mater. 56 (2007) 669–672.
[33] M. Long, J. Jiang, Y. Li, R. Cao, L. Zhang, W. Cai, Nano-Micro Lett. 3 (2011) 171–177.
[34] R. Zanella, S. Giorgio, C.R. Henry, C. Louis, J. Phys. Chem. B 106 (2002) 7634–7642.
[35] E.M. Levin, R.S. Roth, J. Res. Natl. Bur. Stand. A Phys. Chem. 68A (1964) 189–195.
[36] X. Zhang, L. Zhang, J. Phys. Chem. C 114 (2010) 18198–18206.
[37] S. Pei, J. Zhao, J. Du, W. Ren, H.M. Cheng, Carbon 48 (2010) 4466–4474.
[38] M. Long, W. Cai, Z. Wang, G. Liu, Chem. Phys. Lett. 420 (2006) 71–76.
[39] P. Salvador, J. Phys. Chem. C 111 (2007) 17038–17043.
[40] M.R. Hoffmann, S.T. Martin, W. Choi, D.W. Bahnemann, Chem. Rev. 95 (1995) 69–96.